buildings

Article

Tensile Behavior of Basalt-Fiber-Grid-Reinforced Mortar before and after Exposure to Elevated Temperature

Xiaofei Zhang [1], Weidong He [2,*], Yongwang Zhang [3], Cheng Chen [2] and Xun Wu [4]

1 Key Laboratory of C & PC Structures Ministry of Education, Southeast University, Nanjing 210096, China
2 School of Civil Engineering and Geomatics, Southwest Petroleum University, Chengdu 610500, China
3 College of Civil Engineering, Nanjing Tech University, Nanjing 211816, China
4 School of New Materials and Chemical Engineering, Guang'an Vocational & Technical College, Guang'an 638000, China
* Correspondence: hewd@swpu.edu.cn

Abstract: This paper presents an experimental study on the tensile behavior of basalt-fiber-grid-reinforced mortar (BGRM) before and after exposure to an elevated temperature of 300 °C considering the effect of fiber grid type, short polyvinyl alcohol fiber (PVA), and high-temperature exposure time. The experimental results show that the mortar plates reinforced with woven textile T25 and fiber-reinforced polymer (FRP) grid G50 exhibited more pronounced strain-hardening behavior. The highest peak stress was obtained for the T25-reinforced plate, which was 85% and 32% higher than that of the T5- and G50-reinforced plates, respectively. Meanwhile, the bridging effect of PVA fibers in mortar can improve the tensile properties. As the high-temperature exposure time increased, the cracking and peak stress of BGRM decreased significantly. Especially for the T5-reinforced plate after exposure to elevated temperature for 2 h, the cracking and peak stress decreased by 60.5% and 38%, respectively. The positive effect of short PVA fibers on the tensile properties of the BGRM became obsolete owing to the melting of short fibers at high temperature. Furthermore, an exponential strength degradation model related to high-temperature exposure time was proposed.

Keywords: basalt fiber grid; mortar; tensile behavior; elevated temperature; strength degradation

check for updates

Citation: Zhang, X.; He, W.; Zhang, Y.; Chen, C.; Wu, X. Tensile Behavior of Basalt-Fiber-Grid-Reinforced Mortar before and after Exposure to Elevated Temperature. *Buildings* **2022**, *12*, 2269. https://doi.org/10.3390/buildings12122269

Academic Editor: Marco Di Ludovico

Received: 29 November 2022
Accepted: 16 December 2022
Published: 19 December 2022

1. Introduction

Fiber grids have been widely used to reinforce cementitious material due to their advantages of light weight, high strength, and multidirectional reinforcement. The commonly used fiber grid is a multiaxial non-corrosive textile woven with alkali-resistant (AR) glass fiber, carbon fiber, or other fiber, where the polymer is usually used to impregnate the textile to improve its tensile strength [1–3]. The cementitious material reinforced by textile exhibited high tensile strength, excellent strain-hardening behavior, and a multiple-cracking characteristic, which can be applied to strengthen structural members and prefabricate thin-walled members [4,5]. In order to realize the reliable application of the textile-reinforced cementitious material in engineering, numerous studies have been conducted to evaluate the tensile and bending properties, where the stress–strain relationship, tensile/bending strength, and cracking and failure modes were discussed in detail [6–10]. Another kind of grid reinforcement material is a fiber-reinforced polymer (FRP) grid, whose polymer content is much higher than that of textile and which can also be used to reinforce the cementitious material. Some research in relation to the FRP grid mainly focused on strengthening old structural members [11,12]. All of the above research considered the application of fiber grid reinforcement materials at ambient temperature. Generally, owing to the possibility of sudden disasters occurring in practical projects, the structural element may suffer a fire during its service life. As is well known, the mechanical properties of traditional-fiber-reinforced polymer composites degrade significantly at elevated temperatures due to the decomposition of the polymer and the oxidation of fiber [13,14]. A fiber-grid-reinforced cementitious matrix exhibited lower flammability and better high-temperature resistance owing to the inorganic nature of the cementitious material, which made it more suitable for applications in structures subjected to fire [15,16]. Therefore, it was important to investigate the effect of elevated temperature on fiber-grid-reinforced cementitious material for reliable application under fire.

Several studies have been carried out regarding the residual properties of textile-reinforced cementitious material after exposure to different high temperatures [15,17–22]. The tensile test on mortar reinforced with one-layer AR-glass/carbon/carbon textile after exposure to high temperatures for 1 h showed that the mechanical properties of the specimen essentially remained unchanged before 200 °C, and then the strength dropped significantly when the temperature increased to 400 and 600 °C [17]. The effects of high temperature on the behavior of five-layer-impregnated basalt-textile-reinforced refractory concrete were studied by Rambo et al. [20,21], where the specimen was heated up to the maximum temperature of 1000 °C at a heating rate of 10 °C/min. The experimental results show that the fiber–matrix bonding properties were improved at 150 °C due to the re-stiffening mechanism of the impregnation polymer. This phenomenon was different from the tensile properties of the unimpregnated PBO-textile-reinforced mortar after exposure to a high temperature of 100 or 200 °C [15], where the interfacing bond strength between fiber and the cement matrix decreased. Moreover, for different fabric-reinforced mortar plates at a temperature of up to 80 °C, it has been found that the effect of temperature variations on the uncracking stage of mortar was more evident, whereas it had no obvious influence on the post-cracking stage [19]. This was mainly because the fiber bearing the load in the post-cracking stage had excellent high-temperature resistance. The bending behavior of textile-reinforced concrete thin plates after exposure to high temperature for 1 h was performed by Xu et al. [18], where the specimen was heated up to the maximum temperature of 800 °C at a heating rate of 10 °C/min. The test results indicate that the degradation of the mechanical properties of the plate after exposure to elevated temperature was attributed to the decrease in the tensile strength of filaments, the increase in pore size in concrete, and the decreasing bond strength. In addition, the influence of short fibers in the cementitious matrix on the residual tensile behavior of textile-reinforced concrete after exposure to high temperatures was investigated [22].

Structures in practical engineering were subjected to fire and mechanical loads at the same time. Some researchers have investigated the simultaneous mechanical and high-temperature loadings on the properties of cementitious material reinforced by textile [23–26]. A comparative study of the thermomechanical and residual behavior of textile-reinforced concrete showed that the tensile strength and maximum axial strain of textile-reinforced concrete after high-temperature exposure for 1 h were higher than those in hot conditions [24,26]. This was mainly because the softening of impregnating materials under high temperature reduced the interfacial bond strength between the fiber grid and cement matrix. Moreover, the anchoring effect provided by the transverse yarn in the fiber grid was also weakened. An experimental study on the thermomechanical behavior of chopped strand mat glass textile and grid glass textile reinforced concrete showed that the latter had more excellent properties when sustaining the tensile load and high temperatures for 1 h [23]. Moreover, the addition of short glass fiber can improve the thermomechanical behavior of glass-textile-reinforced concrete when the temperature was below 300 °C [25]. In addition, Thomas et al. [27] investigated the effect of BFRP grid reinforcement on the spalling behavior of high-performance concrete thin plates at high temperatures.

The existing research mainly focused on the influence of different target temperatures on the mechanical properties of fiber-grid-reinforced cementitious material. However, there is little published information on the mechanical properties of composites experiencing different high-temperature exposure times. In the fire safety design [28], the fire-exposure time was usually used as a quantitative indicator to ensure the integrity and stability of the building within the specified fire-exposure time. Therefore, it was necessary to study the influence of exposure time on the mechanical properties of fiber-grid-reinforced cementitious material when experiencing elevated temperature.

Basalt fiber has been increasingly used as a reinforcement material over the last decades due to its low-cost and environmentally friendly characteristics. It has a lower price than carbon fiber, and its mechanical properties are comparable to glass fiber. Moreover, basalt fiber exhibited higher thermal stability and heat resistance than glass fiber [29–31], which is more suitable for applications at high temperature. In this study, tensile tests of basalt-fiber-grid-reinforced mortar (BGRM) before and after exposure to elevated temperature were conducted considering the effect of fiber grid type, short PVA fiber, and high-temperature exposure time. Three kinds of fiber grids (T5, T25, and G50), two high-temperature exposure durations (1 and 2 h), and short PVA fiber (volume fraction 1%) were selected as the test parameters. The test results were analyzed in terms of the stress–strain curve, cracking and failure mode, strength utilization efficiency, crack stress, and peak stress. Furthermore, an exponential strength degradation model related to high-temperature exposure time was proposed. This paper may be a valuable reference for the future fire resistance designs of fiber-grid-reinforced cementitious material.

2. Experimental Program

2.1. Materials

Three kinds of basalt fiber grids commonly used in current civil engineering were adopted in this experiment, namely basalt fiber leno textile T5, basalt fiber woven textile T25, and basalt-fiber-reinforced polymer (BFRP) grid G50, as shown in Figure 1. The production process of the basalt fiber textile and BFRP grid was quite different. The textiles were formed through weaving the fibers with a warp knitting machine and then impregnated with the polymer (such as flexible or rigid polymers), while the BFRP grid was manufactured by fully impregnating fibers with the resin (such as epoxy resin) and then made in mold pressing technology. The basalt fiber leno textile T5 was woven by a warp knitting machine along the warp direction, where the mesh size was 5 mm $\times$ 5 mm. The weft yarns of the T5 were straight, where the linear density was 526 tex (1 tex = 1 g/km). In the warp direction, two twisted yarns crossed the weft yarn for weaving, where the linear density of each twisted yarn was 264 tex. The acrylic emulsion was used as the impregnated polymer for the T5 with a content of 6% (mass fraction). Thus, the textile was usually not fully impregnated, and the impregnation only had the effect of shaping. The schematic diagram of the cross-section of the impregnated yarn was depicted in Figure 2a, where only the external fibers were impregnated with the polymer. Moreover, the collaborative workability of the impregnated fibers was still poor owing to the poor cross-linking properties of the acrylic emulsion. The mesh size of the T25 was 25 mm $\times$ 25 mm, where the warp and weft yarns had two straight bundles with a linear density of 2000 tex. The warp yarns were stacked on the weft yarns at the textile nodes, and the textile was woven along the warp direction with the braided wire. Polyvinyl chloride (PVC) was used as the impregnated polymer for the T25 with a content of 11% (mass fraction), and only the external fibers of the yarn were impregnated (Figure 2b). The mesh size of the G50 was 50 mm $\times$ 50 mm, where the impregnation polymer was thermosetting epoxy resin. Both the longitudinal and horizontal single-reinforcement ribs contained fibers with a linear density of 3600 tex, and the impregnation polymer content in the single-reinforcement rib was 73% (mass fraction). So the yarn was fully impregnated with the epoxy resin (Figure 2c). In addition, the resin had strong cross-linking properties after curing, which can ensure the fibers of yarn will transfer load cooperatively.

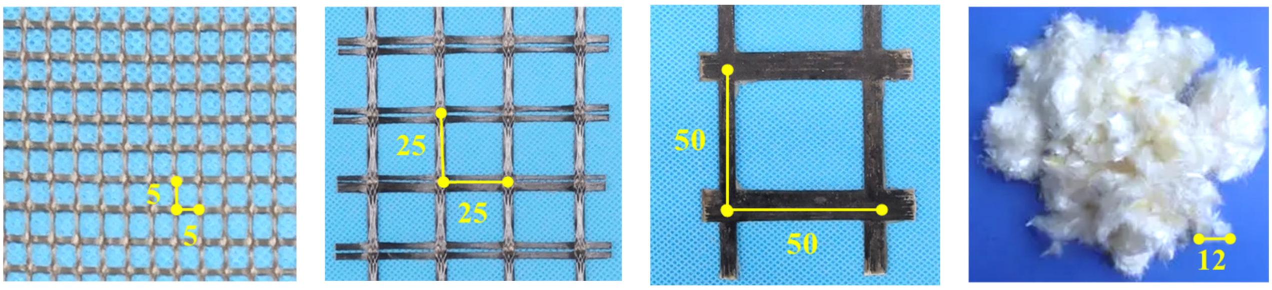

(**a**) (**b**) (**c**) (**d**)

Figure 1. Basalt fiber grid and short PVA fiber (unit: mm): (**a**) T5; (**b**) T25; (**c**) G50; (**d**) short PVA fiber.

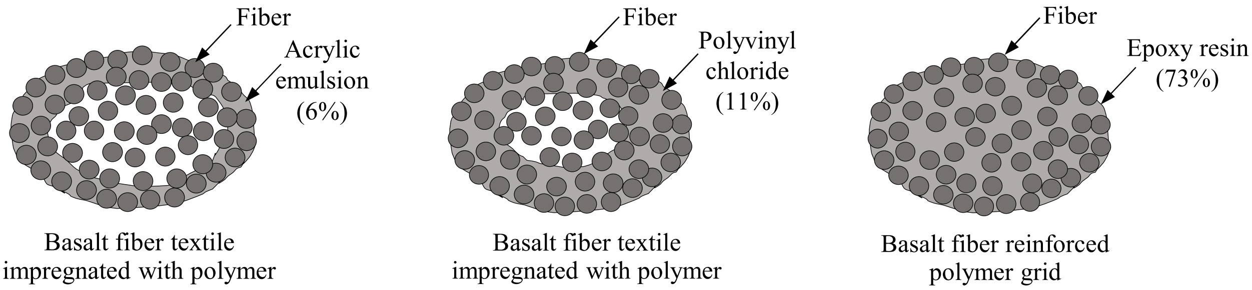

(**a**) (**b**) (**c**)

Figure 2. Schematic diagram of the grid cross-section: (**a**) T5; (**b**) T25; (**c**) G50.

As for the basalt fiber, the density was 2.65 g/cm^3. Then, the effective cross-sectional area of the fiber grid can be obtained, where the effective cross-sectional area referred to the area of the fibers in the grid. The basic mechanical properties of the three basalt fiber grids are listed in Table 1. The tensile test of fiber grid with dimensions of 400 mm × 100 mm (length × width) was conducted by the manufacturer, where the aluminum sheets were used as the clamp materials. The tensile strength of the fiber grid was obtained by dividing the load by the cross-sectional area of the fibers along the tensile direction. It can be noticed that their tensile strengths were quite different. The T5 had the lowest tensile strength, while the G50 had the highest tensile strength. According to the specification (ISO 10618: 2004) [32], the tensile strength of the basalt fiber measured in this experiment was 2830 MPa. So that the fiber strength utilization efficiency k_G for three grids can be calculated, which was the ratio of the tensile strength of grid and tensile strength of fiber, as shown in Figure 3. The value of k_G for the T5 was only 24.5% due to the low cross-linking strength of the polymer and insufficient impregnation. Because the content of impregnated polymer of the T25 was higher than that of the T5, the value of k_G for the T25 was 58.2%, which was higher than that of the T5. The G50 had the highest k_G value of 78.3% as a result of the full impregnation and high cross-linking strength of the epoxy resin.

Table 1. Properties of the basalt fiber grid.

Basalt Fiber Grid	Mesh Size (mm)	Cross-Sectional Area of Fibers in the Grid (mm^2)	Tensile Strength (MPa)	Elastic Modulus (GPa)	Ultimate Strain (%)
T5	5 × 5	3.98	694 (21.4)	32.6 (1.7)	2.7 (0.31)
T25	25 × 25	6.04	1647 (126.4)	74.6 (5.2)	2.4 (0.08)
G50	50 × 50	2.72	2217 (150.3)	93.4 (7.8)	2.3 (0.12)

Note: The values in parentheses are standard deviations.

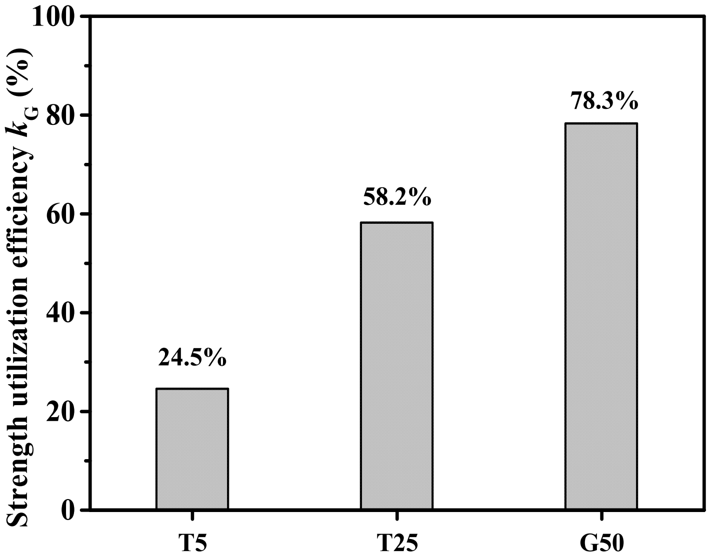

Figure 3. Strength utilization efficiency k_G.

The cementitious material adopted in this work was the cement mortar commonly used in repairing and strengthening the structural components, which were produced by Goodbond Co., Ltd., Changsha, China. The cement mortar was composed of Portland cement, silica sand, mineral additives (fly ash and silica fume), admixture (water reducer and defoamer), polymer, and water. The consistency of the mortar was low, and it had good flowability to ensure that the mortar passes through the mesh of the fiber grid. The size of specimen for testing the strength of mortar was 160 mm in length, 40 mm in width, and 40 mm in thickness. The mortar specimens were cast and then cured for 28 days under standard conditions (temperature 20 °C, humidity over 95%) for the mechanics experiment. The compressive and flexural strength of the mortar block measured was 47.4 MPa and 9.1 MPa, respectively. In addition, 1% (volume fraction) short PVA fibers were added to the mortar to study the effect of short fibers on the tensile properties of the BGRM before and after exposure to elevated temperature. The diameter of the short PVA fiber was 15 µm, and the length was 12 mm, as shown in Figure 1d.

2.2. Specimen Preparation and Test Set-Up

The tensile properties of the BGRM were studied in the form of thin plate, which had the following dimensions: length of 400 mm, width of 100 mm, and thickness of 10 mm. The plate was cast by the layer-laying method through the wooden formwork. First, a 5 mm thick mortar was poured. Subsequently, one layer of grid was laid on the wooden formwork and fixed at the edge. Finally, the upper mortar with a thickness of 5 mm was poured. After the cast plate was vibrated evenly, it was cured for 28 days under standard conditions (temperature 20 °C, humidity over 95%).

The elevated-temperature exposure of the BGRM plate was completed using a high-temperature box resistance furnace (Figure 4a), which consisted of a support, a firebrick furnace, and a temperature controller. The furnace was heated with the resistance wire, and the temperature can be controlled with the electric furnace temperature controller. The schematic diagram of the furnace and the placement of the specimens is presented in Figure 4b. Resistance wires were arranged around the outside of the firebrick furnace, which can ensure that the temperature around the furnace was uniform. The inner dimension of the firebrick furnace was 500 × 300 × 200 mm (length × width × height). In each thermal cycle, three specimens were laid horizontally along the length of the furnace. The cushion blocks were used to support the specimens to ensure that the upper and lower surfaces of the specimens can be heated evenly. The maximum temperature of 1000 °C can be obtained in the furnace. It has been confirmed that the mechanical properties of the textile-reinforced cementitious material degraded significantly when the temperature was above 300 °C and then became brittle when it increased up to 400 °C [19,20]. Meanwhile, 10 °C/min was chosen as a commonly used heating rate for the high-temperature test through a high-temperature box resistance furnace [19–21,24]. The fire-exposure durations of 1 and 2 h are fire resistance ratings used in the fire resistance design of building components [33]. In addition, owing to the small thickness of the test plate, it was assumed that the temperature of the air within the furnace was essentially equal to that in the plate [19–21]. Therefore, the target temperature of 300 °C was adopted in this study, and the elevated-temperature exposure durations were 1 and 2 h, respectively. In heating experiment, the furnace was heated to the temperature of 300 °C with a heating rate of 10 °C/min, and then the target temperature of 300 °C was kept stable for 1 or 2 h. After the target exposure time was reached, the specimens were taken from the furnace and cooled down at ambient conditions. Figure 4c presents the heating regimes.

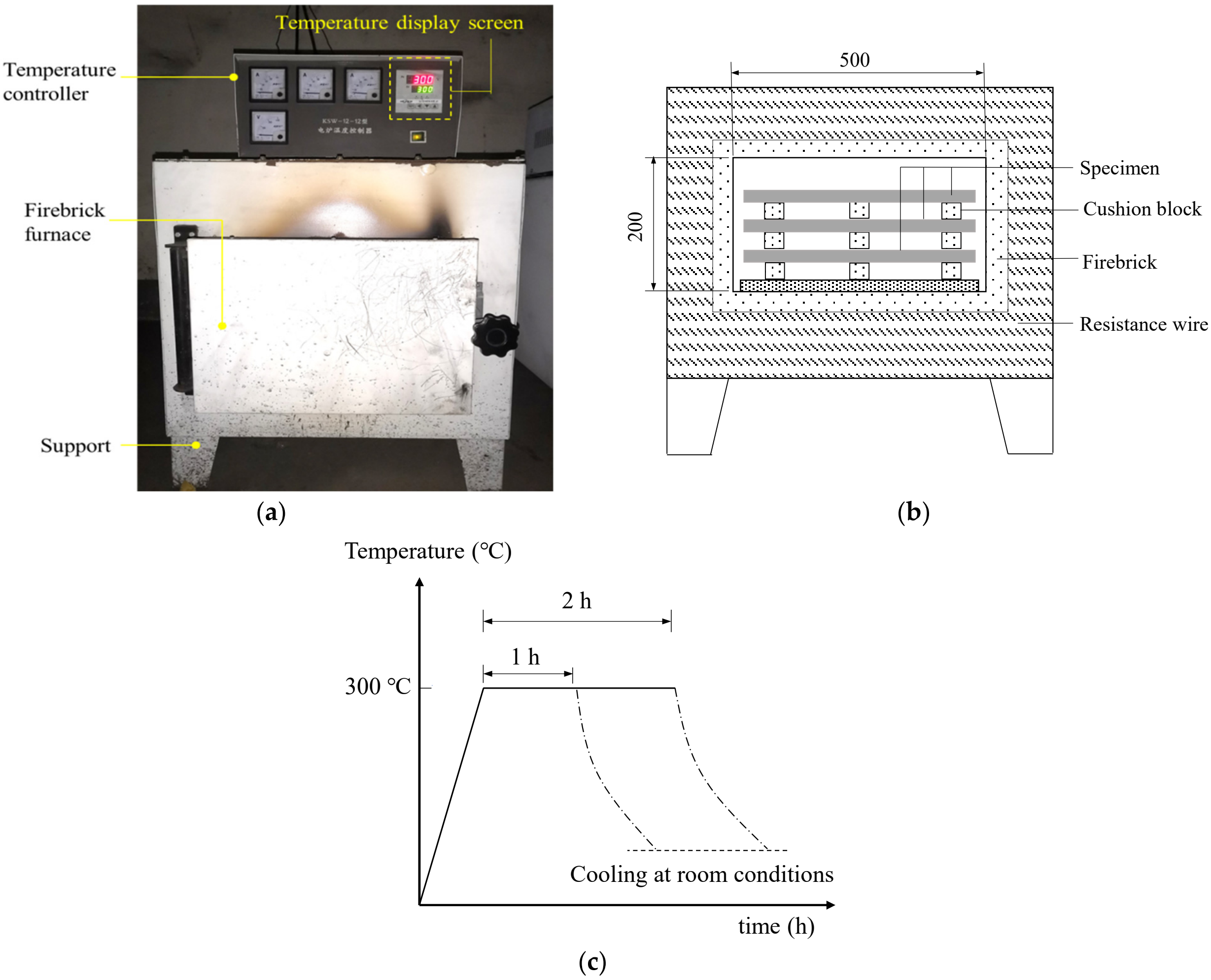

Figure 4. Description of elevated-temperature test procedure (unit: mm): (**a**) high-temperature box resistance furnace; (**b**) schematic diagram of furnace; (**c**) heating regimes.

A testing machine with the maximum load of 1000 kN was used for conducting the tensile test. The displacement rate of 2 mm/min was used in this tensile test. The load was recorded automatically with the testing machine. The tensile displacement was measured with a laser displacement sensor with the gauge length of 200 mm and recorded with 24-bit high-precision USB data acquisition equipment (Figure 5a). In addition, a hinged connection was designed for tensile test to ensure that the forces on both ends of the plate were aligned in a straight line, as displayed in Figure 5b. The steel plate B was glued on the end of plate with epoxy resin. Then, steel plate A and steel plate B were connected with a bolt. The upper and lower fixtures of the testing machine clamped steel plate A and applied a tensile load to the specimen.

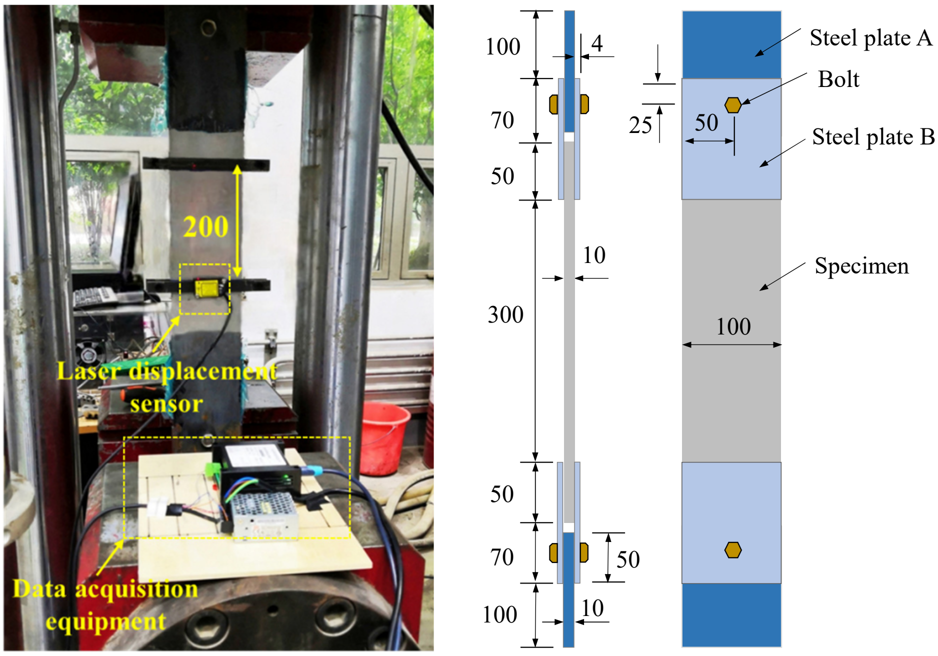

(**a**) (**b**)

Figure 5. Tensile test set-up and specimen dimensions (unit: mm): (**a**) tensile test set-up; (**b**) specimen dimensions.

Tensile tests were performed on the mortar plates reinforced with three different basalt fiber grids at ambient temperature and after exposure to high temperature of 300 °C for 1 and 2 h. At the same time, tensile tests were conducted on the BG50 and short-PVA-fiber-reinforced mortar plate. Three specimens were tested for each research parameter. A total of 36 specimens were tested in this study, as presented in Table 2. In the specimen number, the letter combination "BT" stands for the basalt fiber textile. The letter combination "BG" stands for the BFRP grid. The first Arabic number after the letter stands for the dimension of mesh. The letter "F" stands for the short PVA fibers which are added to the mortar matrix. The letter combination "CT" represents the control temperature (ambient temperature 20 °C). The second Arabic number 300 refers to the target temperature of 300 °C, and the following "1 h" and "2 h" represent the high-temperature exposure time of 1 h and 2 h, respectively.

Table 2. Details of tensile specimens.

BGRM Plate Series	Specimen Number	Grid Type	Reinforcement Ratio (%)	Short PVA Fiber (%)	Temperature T (°C)	Exposure Time t (h)
BT5	BT5-CT BT5-300-1h BT5-300-2h	T5	0.398		20 300 300	 1 2
BT25	BT25-CT BT25-300-1h BT25-300-2h	T25	0.604		20 300 300	 1 2
BG50	BG50-CT BG50-300-1h BG50-300-2h	G50	0.272		20 300 300	 1 2
BG50F	BG50F-CT BG50F-300-1h BG50F-300-2h	G50	0.272	1.0	20 300 300	 1 2

3. Results and Discussions

3.1. Tensile Behavior of BGRM before Exposure to Elevated Temperature

In this section, the tensile behavior of BGRM before exposure to elevated temperatures is analyzed. The failure and cracking modes, characteristics of tensile stress–strain curves, and the comparisons of the plates reinforced with different basalt fiber grids are discussed in detail. The experimental results of the BGRM before exposure to elevated temperatures are summarized in Table 3. Here, the tensile load divided by the cross-sectional area of the plate was defined as the tensile stress, and the elongation of the gauge length for the plate divided by the initial value of gauge length was defined as the tensile strain. P_{cr}, σ_{cr}, and ε_{cr} represented the cracking load, cracking stress, and cracking strain of the tested plate when the first crack occurred, respectively. P_u, σ_u, and ε_u represented the peak load, peak stress, and peak strain of the tested plate after cracking, respectively.

Table 3. Tensile test results of the BGRM before exposure to elevated temperature.

Specimen Number	Cracking Load P_{cr} (N)	Cracking Stress σ_{cr} (MPa)	Cracking Strain ε_{cr} (%)	Peak Load P_u (N)	Peak Stress σ_u (MPa)	Peak Strain ε_u (%)
BT5-CT	4154.3 (4.4)	4.15 (4.4)	0.46 (6.7)	3505.8 (7.3)	3.51 (7.3)	0.84 (1.1)
BT25-CT	3961.4 (17)	3.96 (17)	0.41 (7.9)	6503.5 (1.6)	6.50 (1.6)	3.54 (6.7)
BG50-CT	3487.1 (8.7)	3.49 (8.7)	0.46 (22)	4936.5 (5.2)	4.94 (5.2)	3.31 (10)
BG50F-CT	4640.2 (13)	4.64 (13)	0.37 (3.3)	5702.3 (0.9)	5.70 (0.9)	1.88 (9.8)

Note: The value in parentheses is the coefficient of variation (%).

3.1.1. Failure and Cracking Modes

Figure 6 shows the typical tensile failure and cracking modes of the BGRM at ambient temperature. For the thin plate BT5-CT, only one main crack appeared when it failed (Figure 6a). The crack was located in the middle of the plate or near the anchoring end, and the textile finally fractured completely. Multiple cracks appeared on the thin plates BT25-CT and BG50-CT when they failed (Figure 6b,c). The number of cracks was between five and six, and the plate finally broke near the anchoring end. Some fractured fibers can be observed from the broken surface of the plate. Moreover, it can be noted that the cracking modes of the thin plate were closely related to the bearing capacity of the grid. As the bearing capacity of the fiber grid increased, the more obvious multi-cracking pattern developed in the plate. In addition, compared with the BG50-CT plate, the cracks of the plate with the addition of short PVA fibers in the matrix became denser. As for the thin plate BG50F-CT, owing to the bridging effect of the short PVA fibers in the matrix, more micro-cracks were observed during the tensile process. However, some micro-cracks closed due to the unloading of the broken plate, and finally, about eight cracks could be seen on the surface of the thin plate (Figure 6d).

3.1.2. Tensile Stress–Strain Curves

Figure 7 presents the tensile stress–strain curve of the BGRM plate at ambient temperature. As for the BT5-CT (Figure 7a), the stress rose linearly with the strain increasing before the plate cracked, where the most load was born by the mortar. After cracking, the stress first dropped sharply and then gradually increased with the strain increasing. When the tensile strength of the textile was reached, a sudden drop occurred in the stress, and eventually, the textile broke. No obvious strain hardening was observed. Due to the low overall bearing capacity of the textile in the BT5-CT, the stress fluctuation range was large during the entire tensile process. Moreover, few fluctuation peaks appeared on the stress–strain curve, which corresponded to the cracking mode of the plate. For the thin plates BT25-CT and BG50-CT (Figure 7b,c), the pronounced strain-hardening behavior was observed. The stress drop after cracking was relatively small, and the stress of the mortar was transferred to the grid at the crack. Owing to the high bearing capacity of the grid, the grid did not fracture when carrying the suddenly increasing stress. As the applied strain increased, the stress in the grid reinforcement increased and continued to be transferred to the uncracked area of the matrix due to the bond between the grid and mortar, which caused the new crack to appear, and the stress decreased again. After repeating this process, more cracks formed in a multiple-cracking pattern, and many fluctuation peaks appeared on the post-crack stage of the stress–strain curve. Finally, the matrix fully cracked, and the grid carried the load alone until the tensile strength was reached, and then the stress dropped sharply. A final linear branch took place on the stress–strain curve, in which no further cracks developed on the plate. Furthermore, in the case of the BGRM with the PVA short fibers added to the mortar, the stress fluctuation became insignificant as a result of the bridging effect of the fiber in the matrix. The plate cracked more stably, as shown in Figure 7d. The stress did not decrease significantly after the first crack appeared, and the amplitude of stress fluctuation in the post-cracking stage was small, which was consistent with the cracking mode observed in the test. Compared with the thin plate BG50-CT, more micro-cracks appeared in the BG50F-CT during the tensile process. This suggested that adding short fibers to the mortar can stabilize the stress development in the post-cracking stage.

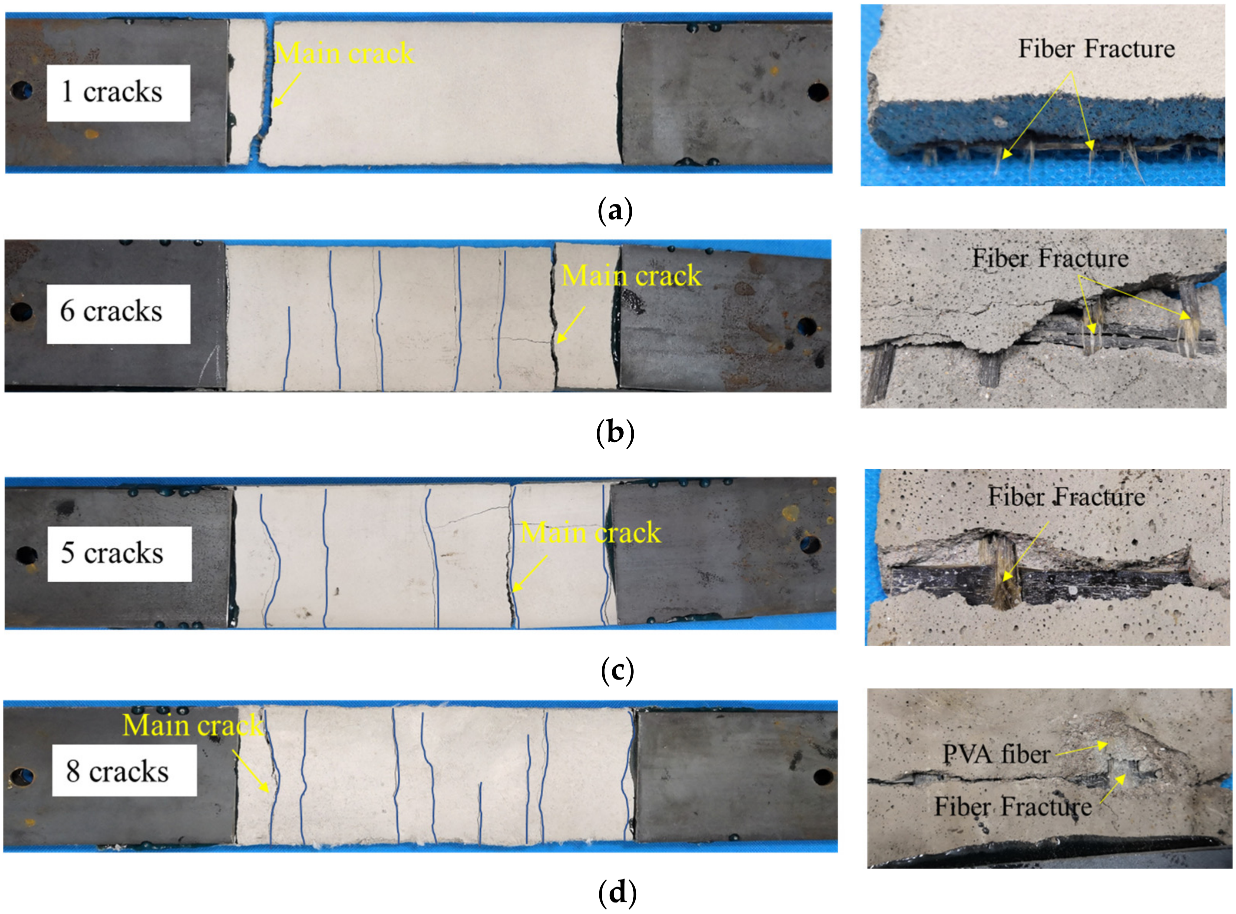

Figure 6. Failure and cracking modes of the BGRM before exposure to elevated temperature: (**a**) BT5-CT; (**b**) BT25-CT; (**c**) BG50-CT; (**d**) BG50F-CT.

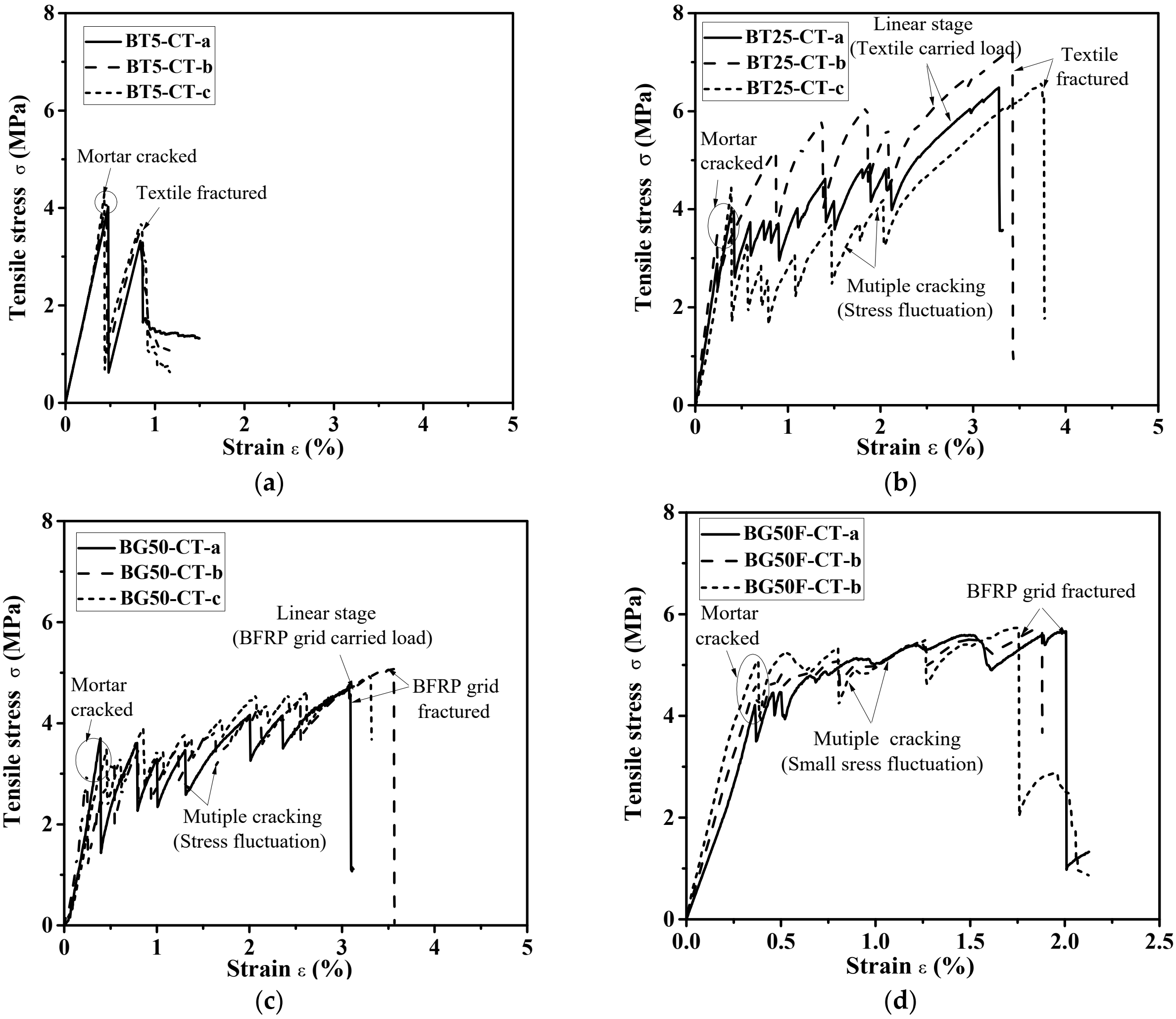

Figure 7. Tensile stress–strain curves of the BGRM before exposure to elevated temperature: (**a**) BT5-CT; (**b**) BT25-CT; (**c**) BG50-CT; (**d**) BG50-CT.

3.1.3. Comparison of the BGRM Reinforced with Different Basalt Fiber Grids

Figure 8a shows the tensile cracking stress and peak stress of the BGRM at ambient temperature. For the BGRM plate, the load was mainly carried by the mortar matrix before cracking, and the load carried by the internal grid reinforcement can be ignored. Therefore, the cracking stress of different fiber-grid-reinforced mortar plates was close, where the values were generally distributed between 3.5 MPa and 4.2 MPa. The slight difference in the cracking stress may be caused by the defects in the mortar plate. Furthermore, it can be found that the type of the fiber grid had a significant influence on the peak stress, where the peak stress was mainly determined by the whole bearing capacity of the fiber grid in the BGRM plate. The thin plate BT5-CT had the lowest peak stress of 3.51 MPa, which was 15% lower than the cracking stress, indicating that one layer of textile T5 had no enhancement effect on the tensile strength of the mortar. The thin plate BT25-CT had the most obvious enhancement effect on the mortar, with the highest peak stress of 6.5 MPa, which was 64% higher than the cracking stress. The peak stress of the thin plate BG50-CT was 4.94 MPa, which was 42% higher than the cracking stress. In addition, compared with the BG50-CT, the cracking stress and peak stress of the BG50F-CT increased by 33% and 15%, respectively. This was mainly attributed to the bridging effect of the short PVA fibers in the mortar. The addition of short PVA fiber was not only beneficial to the cracking stress but also can make the matrix and grid cooperate well with each other in the post-cracking stage, which can increase the peak stress of the plate.

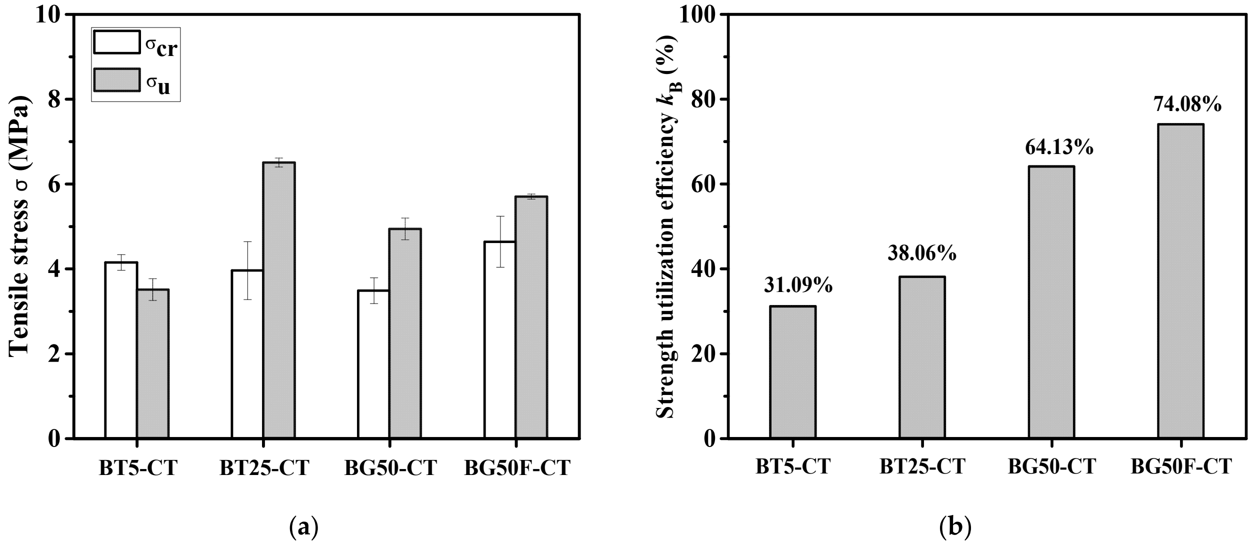

Figure 8. Tensile behaviors of the BGRM before exposure to elevated temperature: (**a**) tensile stress; (**b**) strength utilization efficiency k_B.

Based on the above analysis of tensile stress–strain curves for the BGRM, it can be found that the mortar matrix could not bear the load when the plate approached the failure, and only the fiber grid bore the load. Therefore, the tensile strength of the grid in the plate can be further calculated. The ratio of tensile strength for the fiber grid in the plate to the tensile strength of the fiber was defined as the fiber strength utilization efficiency k_{B} for the grid in the BGRM plate, as shown in Figure 8b. Obviously, the BT5-CT had the lowest strength utilization efficiency k_{B} of 31.09%. The value of k_{B} for the BT25-CT was slightly higher than that of the BT5-CT, which was 38.06%. The BG50-CT had the highest k_{B} value of 64.13%, which was 106% higher than that of the BT5-CT. This suggested that the strength of the basalt fiber can be more fully exerted when the BFRP grid was used to reinforce the mortar. Meanwhile, the addition of short PVA fibers to the mortar was conducive to the improvement of the k_{B}. Compared with the thin plate BG50-CT, the value of k_{B} for the BG50F-CT was improved by 16%.

Figure 9 presents the comparison results of the strength utilization efficiency k_{G} and k_{B} of the grid. It can be noticed that for the T25 and G50, the value of k_{B} was lower than that of k_{G}. While for the T5, the values of k_{G} and k_{B} were 24.5% and 31.1%, respectively, where the strength utilization efficiency of the grid in the mortar was improved by 27%. The reason for this phenomenon was that the textile T5 had twisted yarns in the warp direction. The warp yarn would twist when sustaining the tensile load, which had an adverse effect on the tensile strength of the fiber. This has been confirmed in the literature [34]. However, as for the textile T5 in the mortar, the adverse effect of torsion was weakened due to the restraint of the mortar, so an improvement was observed in the value of k_{B}. The difference between the k_{G} and k_{B} was the largest for the textile T25, where the values of k_{G} and k_{B} were 58.2% and 38%, respectively. The fiber strength utilization efficiency for the grid in the plate was reduced by 35%. This can be explained by the poor interfacial bonding between the woven textile and mortar, thus resulting in a further decrease in the fiber strength utilization efficiency. In addition, the uneven stress of the yarn in the woven textile will also cause the fiber strength to be unable to be fully utilized. The minimal difference between the value of k_{G} and k_{B} was observed in the G50, where the values of k_{G} and k_{B} were 78.3% and 64.1%, respectively. The fiber strength utilization efficiency for the grid in the plate was reduced by 18%. This was not only related to the sufficient impregnation of the BFRP grid but also that the node of the BFRP grid was relatively firm. So the grid had an interlocking effect on the mortar, which was beneficial to the exertion of the tensile strength of the fiber grid. Furthermore, the addition of short PVA fibers to mortar can increase the fiber strength utilization efficiency of the grid further. Compared with the k_G, the value of k_B was only reduced by 4%.

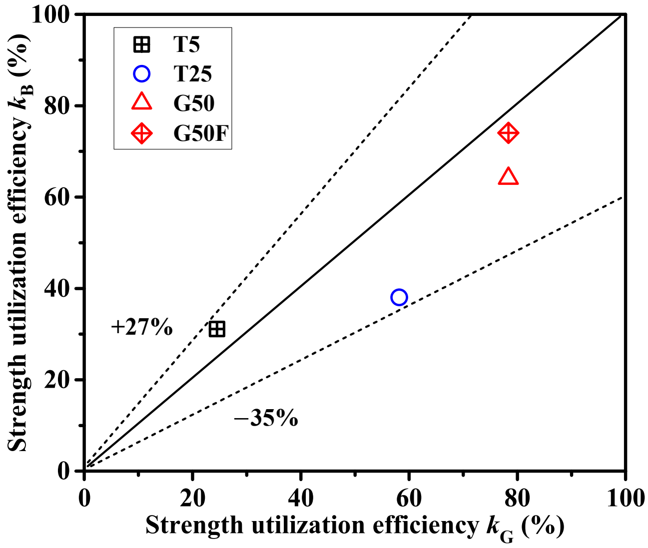

Figure 9. Comparison results of the fiber strength utilization efficiency.

3.2. Tensile Behavior of the BGRM after Exposure to Elevated Temperature

The tensile behavior of BGRM after exposure to elevated temperatures is analyzed in this part. The failure and cracking modes, characteristics of tensile stress–strain curves, and strength degradations are discussed in detail. The experimental results of the BGRM after exposure to elevated temperatures are summarized in Table 4. The calculation methods for the stress and strain were the same as those of the plate before exposure to elevated temperature. The strength degradation coefficient was the ratio of the peak stress of the plate after experiencing elevated temperature to that of the plate at ambient temperature.

Table 4. Tensile test results of the BGRM after exposure to elevated temperature.

Specimen Number	Cracking Load P_{cr} (N)	Cracking Stress σ_{cr} (MPa)	Cracking Strain ε_{cr} (%)	Peak Load P_u (N)	Peak Stress σ_u (MPa)	Peak Strain ε_u (%)	Degradation Coefficient
BT5-300-1h	2293.1 (16)	2.29 (16)	0.28 (16)	2591.7 (9.4)	2.59 (9.4)	1.09 (20)	0.74
BT5-300-2h	1642.7 (13)	1.64 (13)	0.19 (14)	2148.5 (3.9)	2.15 (3.9)	0.51 (27)	0.61
BT25-300-1h	2660.9 (13)	2.66 (13)	0.25 (7.2)	5409.5 (13)	5.4 (13)	2.50 (15)	0.83
BT25-300-2h	1942.2 (15)	1.94 (15)	0.30 (5.3)	4916.0 (15)	4.92 (15)	2.34 (11)	0.75
BG50-300-1h	1982.2 (7.5)	1.98 (7.5)	0.46 (2.7)	4478.2 (11)	4.48 (11)	2.21 (9.2)	0.91
BG50-300-2h	1897.3 (1.0)	1.90 (1.0)	0.18 (24)	3818.2 (13)	3.82 (13)	1.52 (16)	0.77
BG50F-300-1h	3050.8 (11)	3.05 (11)	0.24 (18)	4404.2 (12)	4.40 (12)	2.27 (8.9)	0.89
BG50F-300-2h	2348.1 (6.1)	2.35 (6.1)	0.23 (17)	3990.3 (3.4)	3.99 (3.4)	1.12 (1.5)	0.70

Note: The value in parentheses is the coefficient of variation (%).

3.2.1. Failure and Cracking Modes

The BGRM after exposure to elevated temperature broke in the region near the middle or anchoring end of the plate. Moreover, there was not an obvious difference in the cracking mode of the plate after exposure to elevated temperature for 1 or 2 h. Therefore, the typical failure and cracking modes of the BGRM plate after exposure to 300 °C for 2 h were analyzed, as presented in Figure 10. The thin plate BT5-300-2h broke with one crack (Figure 10a), which was similar to the plate at ambient temperature. Compared with the BT25-CT, no obvious decreases in the number of cracks were observed for the BT25-300-2h (Figure 10b). Moreover, it can be seen from the fractured sections of the BT5-300-2h and BT25-300-2h that the filaments in the broken grid were loose due to the decomposition of the impregnated polymer under the elevated temperature. This will make it difficult for the fibers in the grid to transfer the load cooperatively. In addition, no visible changes occurred in the color of the mortar after exposure to the elevated temperature. The BG50-300-2h still broke with multiple cracks developing (Figure 10c), where the number of cracks was fewer than that of the plate at ambient temperature. The fracture section showed that obvious damage appeared on the surface of G50 as a result of the decomposition of the epoxy resin at elevated temperature. Similarly, the number of cracks on the surface of BG50F-300-2h decreased significantly compared with that of BG50F-CT, as presented in Figure 10d. Furthermore, similar cracking modes can be seen for the BG50-300-2h and BG50F-300-2h. This suggested that adding short PVA fibers to the mortar had little effect on the cracking mode of the BGRM plate at elevated temperature. Because the PVA fibers generally melt between 200 and 300 °C [35], the pores caused by the melted PVA fibers in the PCM can also be seen from the fracture section (Figure 10d).

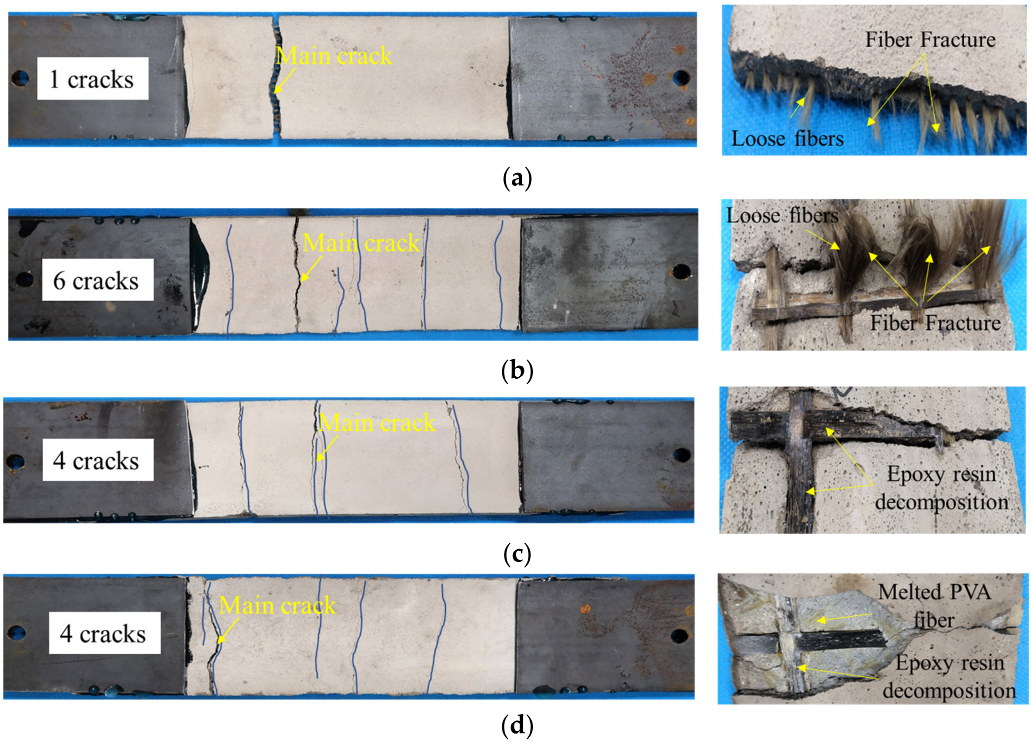

Figure 10. Failure and cracking modes of the BGRM after exposure to elevated temperature: (**a**) BT5-300-2h; (**b**) BT25-300-2h; (**c**) BG50-300-2h; (**d**) BG50F-300-2h.

3.2.2. Tensile Stress–Strain Curves

Figure 11 shows the representative tensile stress–strain curves of the BGRM plate before and after exposure to elevated temperature. As for the thin plate BT5, both the cracking stress and peak stress decreased with the exposure time increasing. The peak stress was greater than the cracking stress for the plate after exposure to 300 °C for 1 or 2 h, as depicted in Figure 11a. The strain-hardening phenomenon can still be observed for the T25- or G50-reinforced mortar plate after experiencing different high-temperature exposure times, while it gradually became less obvious with the exposure time increasing. For the thin plate BT25 (Figure 11b), the stress–strain curve after experiencing high temperature rose linearly before the plate cracked, and the stress fluctuation occurred in the post-cracking stage. Compared with the plate at ambient temperature, the cracking stress and peak stress of the plate decreased after experiencing high temperature. As the high-temperature exposure time increased, the number of stress fluctuation peaks in the post-cracking stage decreased, and the stage in which the grid carried the load alone was missing. The main reason for this phenomenon was that the impregnation polymer in the grid gradually decomposed with the high-temperature exposure time increasing, so that the bearing capacity of the grid and the bond strength between the grid and matrix decreased, which affected the stress development in the post-cracking stage of the thin plate. A similar trend appeared in the stress–strain curve of the thin plate BG50 after exposure to elevated temperature (Figure 11c). Compared with the plate at ambient temperature, fewer stress fluctuation peaks were observed for the plate after exposure to elevated temperature. As for the thin plate BG50F (Figure 11d), the cracking stress and peak stress of the plate decreased after experiencing elevated temperature. The stress change in the post-cracking stage for the plate before exposure to elevated temperature was relatively stable. However, more significant stress fluctuations were observed in those plates after experiencing elevated temperature. This may be attributed to that the short PVA fibers in the mortar were melted under high temperature [35]. So the bridging effect of fiber was weakened, which resulted in a more significant decrease in stress when the crack appeared.

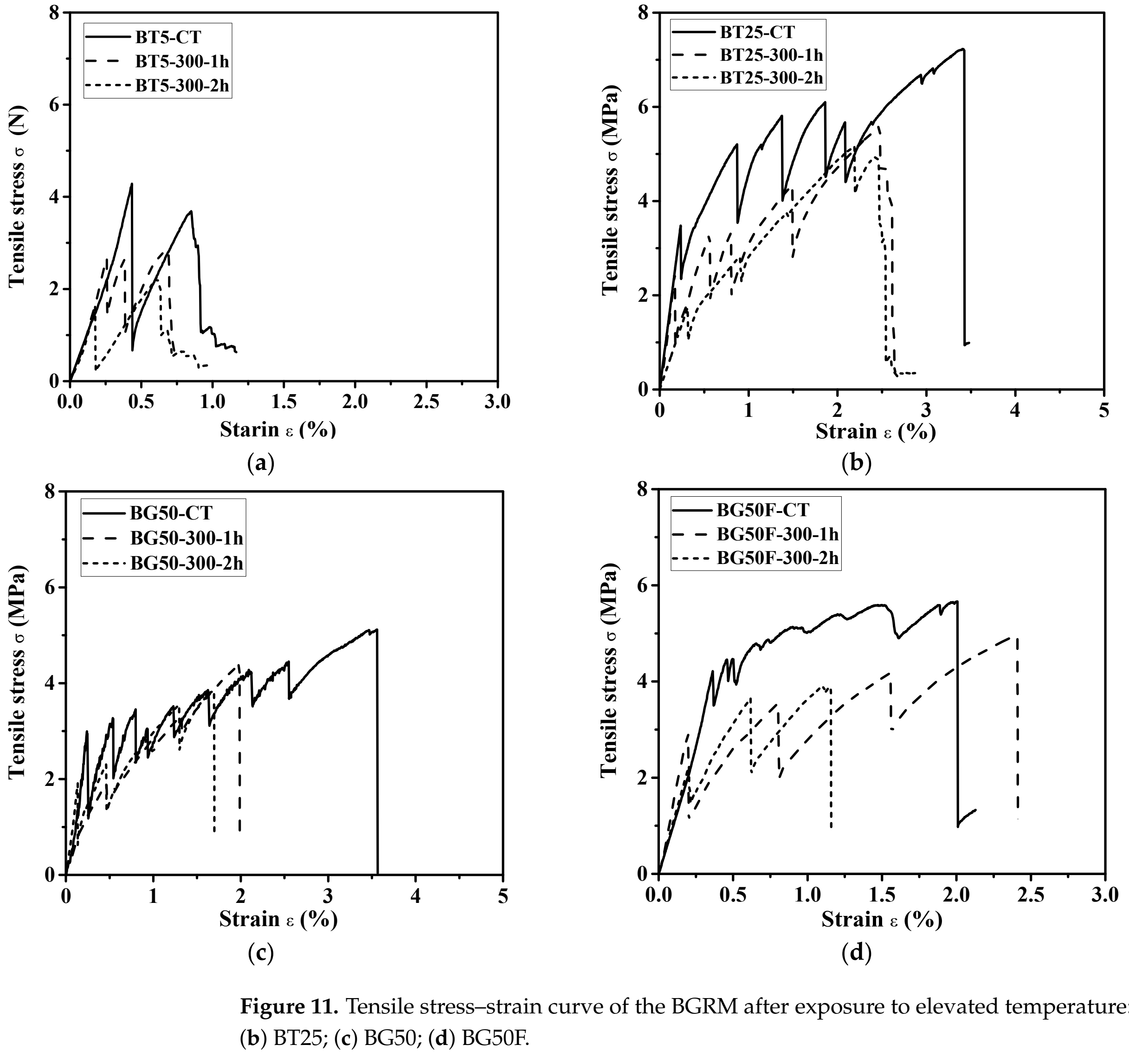

Figure 11. Tensile stress–strain curve of the BGRM after exposure to elevated temperature: (**a**) BT5; (**b**) BT25; (**c**) BG50; (**d**) BG50F.

3.2.3. Degradation of Tensile Behavior of the BGRM

Figure 12 shows the degradation of tensile cracking stress and peak stress for the BGRM after different high-temperature exposure times. As the high-temperature exposure time increased, the degradation laws of the cracking stress for the plates reinforced with different fiber grids were similar, as shown in Figure 12a. The cracking stress decreased significantly after exposure to 300 °C for 1 h, while it decreased gently at the exposure time of 1–2 h. Compared with the plate at ambient temperature, the cracking stress of the thin plates BT5, BT25, BG50, and BG50F after exposure to 300 °C for 1 h decreased by 44.8%, 32.8%, 43.2%, and 34.2%, respectively. As for the plates after exposure to 300 °C for 2 h, the cracking stress of thin plates BT5, BT25, BG50, and BG50F decreased by 60.5%, 51%, 45.6%, and 49.4%, respectively. The degradation of the cracking stress was mainly caused by the evaporation of the bound water in the cement mortar at high temperature and the thermal decomposition of the hardened cement paste. Moreover, the incompatible deformation of the aggregate and shrinkage of the cement paste also led to the decrease in the cracking stress of the matrix [36,37]. In addition, for the BG50F, with the increase in high-temperature time, the cracking stress was gradually close to that of BG50 due to the melting of short PVA fibers at high temperature [35]. The cracking stress of the BG50F was 23.6% higher than that of the BG50 with exposure to 300 °C for 2 h.

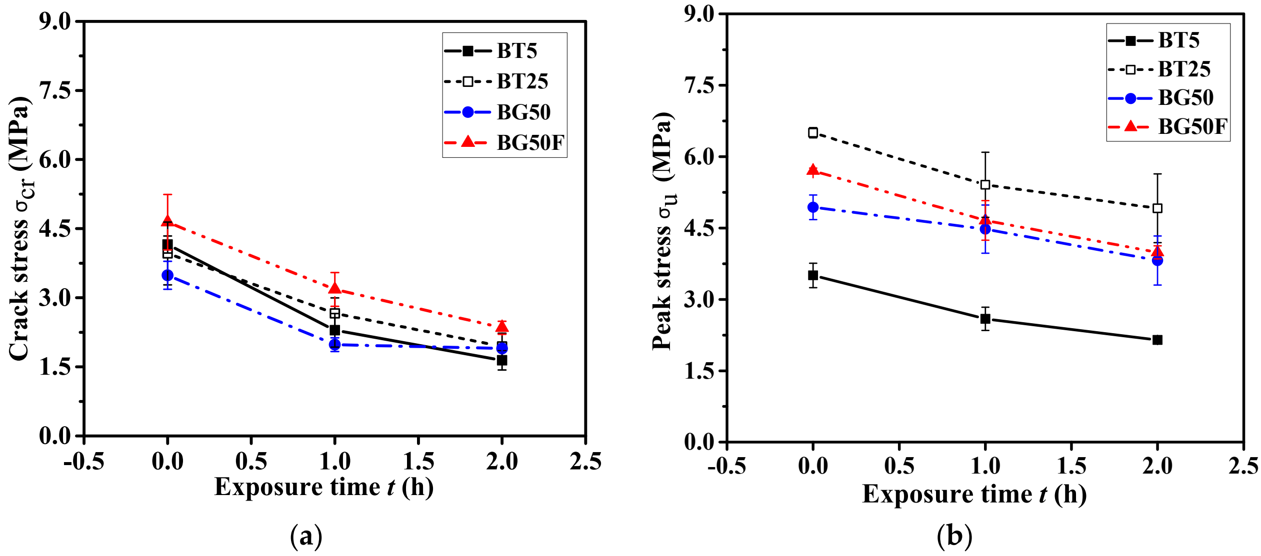

Figure 12. Tensile behaviors of the BGRM after exposure to elevated temperature: (**a**) crack stress; (**b**) peak stress.

Owing to the adverse influences of high temperature on the mechanical properties of the fiber grid and the interface bonding between the grid and mortar, the peak stress of BGRM decreased with the high-temperature exposure time increasing. At high temperature, the impregnated polymer of the grid gradually decomposed, resulting in that the fibers in the grid were unable to transfer the force cooperatively, which reduced the tensile strength of the grid. Meanwhile, due to the decomposition of the impregnated polymer, some gaps appeared between the grid and the mortar, which led to further damage in the interface bonding [38]. The above factors decreased the peak stress of the BGRM. Furthermore, the degradation laws of peak stresses for the plates reinforced with different fiber grids were similar with the high-temperature exposure time increasing (Figure 12b). The peak stress decreased significantly after exposure to 300 °C for 1 h, while it decreased gently at the exposure time of 1–2 h. This can be explained by that the impregnation polymer in the grid decomposed rapidly in the early stage of the high-temperature heating [38]. With the decomposition of the impregnation polymer, the mechanical properties of the BGRM plate mainly depended on the basalt fiber, which had excellent heat resistance [30]. Therefore, the degradation trend became gentle with the exposure time increasing. Compared with the plate at ambient temperature, the peak stress of the thin plates BT5, BT25, BG50, and BG50F after exposure to 300 °C for 1 h decreased by 26.2%, 16.9%, 10.3%, and 22.8%, respectively. As for the plates after exposure to 300 °C for 2 h, the peak stress of the thin plates BT5, BT25, BG50, and BG50F decreased by 38.7%, 24.3%, 22.7%, and 30%, respectively. Moreover, compared with other plates, the BT25 after exposure to elevated temperature had the highest peak stress due to the high bearing capacity of T25. The thin plate BT5 had the lowest peak stress before and after exposure to elevated temperature. As for the plate reinforced with the G50, the addition of the short PVA fibers in the mortar can improve the peak stress of the plate at ambient temperature, while for the plate after experiencing elevated temperature, the short PVA fiber had no obvious effect on the peak stress. The difference in the peak stress of the BG50F and BG50 was within 5% when the high-temperature exposure duration was 1 or 2 h. This was mainly attributed to the melting of PVA fiber at high temperature, and the bridging effect disappeared in the matrix [35]. Thus the collaborative performance of the mortar and grid became worse, and the peak stress of BGRM cannot be effectively improved.

3.2.4. Strength Degradation Model

Based on the above analysis, it was evident that the peak stresses of the mortar plates reinforced with different fiber grids decreased with the high-temperature exposure time increasing. The ratio between the peak stress $\sigma_u(t)$ of the BGRM after experiencing elevated temperature and the peak stress $\sigma_u(t_0)$ of the BGRM at ambient temperature was defined as the strength degradation coefficient D. The strength degradation coefficients of the mortar plates reinforced with different fiber grids are summarized in Figure 13. Therefore, an exponential strength degradation model related to the high-temperature exposure time can be proposed, as shown in Equation (1), where a and τ are fitting parameters.

$$D = \frac{\sigma_u(t)}{\sigma_u(t_0)} = a \cdot \exp(-\frac{t}{\tau}) \tag{1}$$

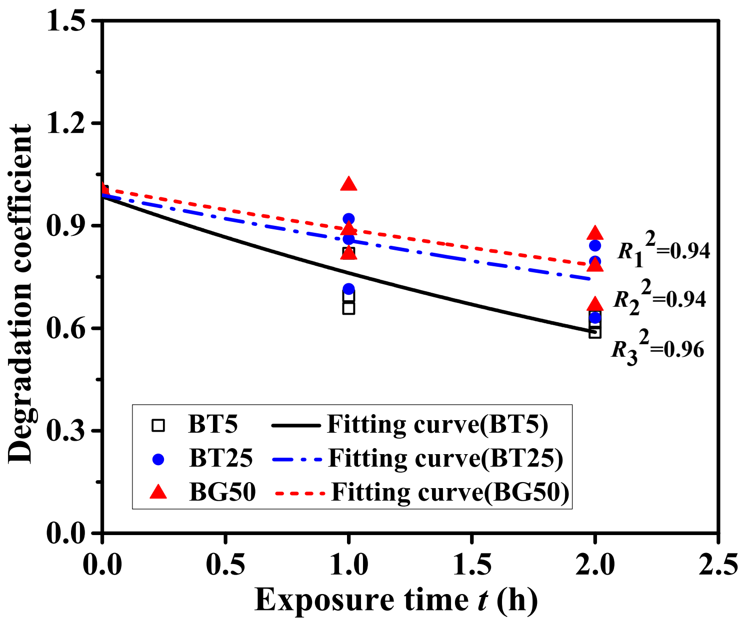

Figure 13. Prediction of strength degradation for the BGRM after exposure to elevated temperature.

The strength degradations of the thin plates BT5, BT25, and BG50 at an elevated temperature of 300 °C were fitted using the exponential model with high fitting accuracy (the tensile properties of the thin plate BG50F after exposure to elevated temperature were similar to that of the BG50, so the strength degradation of the BG50F was not fitted here), as shown in Equations (2)–(4). The fitting correlation coefficients R^2 were 0.94, 0.94, and 0.96, respectively.

$$\text{BT5}: \ D = 0.985 \cdot \exp(-\frac{t}{3.5}) \tag{2}$$

$$\text{BT25}: \ D = 0.989 \cdot \exp(-\frac{t}{6.9}) \tag{3}$$

$$\text{BG50}: \ D = 1.008 \cdot \exp(-\frac{t}{7.9}) \tag{4}$$

The strength degradation of the thin plate BT5 was the fastest, followed by the thin plate BT25, and the thin plate BG50 had the slowest degradation rate, as depicted in Figure 13. The main reason for this phenomenon was that for the thin plate BT5, the impregnated polymer content of the textile T5 was only 6%, which was quickly decomposed at the elevated temperature, so that the peak stress of the plate decreased rapidly with the high-temperature exposure time increasing. As for the thin plate BT25, the degradation of peak stress was relatively slow due to the relatively high impregnated polymer content of the textile T25, where the polymer decomposed relatively slowly with the high-temperature exposure time increasing. As for the BFRP grid G50, the content of the impregnated polymer (epoxy resin) was as high as 73%. Therefore, with the increase in exposure time, although the polymer was decomposed to a certain extent, the residual amount of the polymer was still high, which can ensure the fibers will transfer load cooperatively. Thus, the peak stress degradation of the thin plate BG50 was the slowest. Consequently, the degradation of the tensile behavior of the BGRM plate after exposure to elevated temperature was closely related to the content of the impregnation polymer in the fiber grid.

4. Conclusions

The tensile properties of the BGRM before and after exposure to elevated temperatures were studied in this study. Based on the experimental results, the following conclusions can be drawn:

1. The T25- and G50-reinforced mortar plates at ambient temperature exhibited more cracks and more obvious strain hardening in the post-cracking stage of stress–strain curves. The higher the bearing capacity of the grid, the greater the peak stress of the thin plate. The peak stress for the T25-reinforced plate was 85% and 32% higher than that of the T5- and G50-reinforced plates, respectively. In addition, adding short fibers to the mortar was a good choice to improve the tensile properties of BGRM, where both the cracking and peak stress can be improved.
2. The fiber strength utilization efficiency of the grid was affected by the impregnation polymer. The G50 had the highest strength utilization efficiency of 78.3% when tensioned alone, and the T5 had the lowest value of 24.5%. The epoxy resin was recommended as the impregnated polymer for the high-strength utilization of fiber in the grid. Moreover, the strength utilization efficiency of the T25 and G50 decreased when tensioned in the plate, while the strength utilization efficiency of the T5 was improved due to that the twisted yarn was restrained by the mortar.
3. High-temperature exposure time was the key factor affecting the tensile properties of BGRM. With the high-temperature exposure time increasing, the reinforcement effect of the fiber grid on the mortar was gradually weakened. The strain hardening in the post-cracking stage of the stress–strain curve gradually became less obvious, and the cracking and peak stress decreased significantly. In addition, owing to the melting of short fibers at high temperature, it is undesirable to improve the tensile properties by adding PVA fiber into the mortar.
4. As the high-temperature exposure time increased, the strength degradation coefficient of the BGRM plates decreased rapidly at first and then gradually became gentle. The higher the impregnation polymer content in the fiber grid, the slower the strength degradation of the plate. The slowest strength degradation was observed in the G50-reinforced mortar plate, whose degradation coefficient was 26.2% higher than that of the T5-reinforced plate. Based on the experimental results, an exponential strength degradation model related to the high-temperature exposure time was proposed, which can describe the strength degradation law of the BGRM plates well.

In this study, it should be noted that only the effects of fire-exposure duration at 300 °C on the residual properties of the BGRM were investigated, which can provide a preliminary reference for the fire resistance design of the BGRM. However, the temperature of 300 °C was relatively low, and a higher target temperature needs to be considered. Moreover, the structures are simultaneously subjected to the load and elevated temperature.

Consequently, it is urgent to study the influence of fire-exposure duration at different temperatures on the thermomechanical behavior and residual properties of the BGRM plates in future work.

Author Contributions: Conceptualization, X.Z. and W.H.; methodology, X.Z.; software, X.Z.; validation, X.Z., W.H. and Y.Z.; formal analysis, X.Z.; investigation, X.Z. and W.H.; re-sources, W.H.; data curation, X.Z. and W.H; writing—original draft preparation, X.Z.; writing—review and editing, X.Z., W.H. and Y.Z.; Visualization, Y.Z., C.C. and X.W.; supervision, W.H.; project administration, W.H.; funding acquisition, W.H. All authors have read and agreed to the published version of the manuscript.

Funding: This research was funded by the National Natural Science Foundation of China (No. 52208290), the Natural Science Foundation of Sichuan Province (Nos. 2022NSFSC1046, 2022NSFSC1130), and the Sichuan Mineral Resources Research Center (No. SCKCZY2022-ZC006).

Institutional Review Board Statement: Not applicable.

Informed Consent Statement: Not applicable.

Data Availability Statement: Data are available upon request; to those interested, please contact the corresponding author.

Acknowledgments: The authors thank Binghao Ge for assistance with the experiments and Mengke Lei for valuable discussion.

Conflicts of Interest: The authors declare that there is no conflict of interest.

References

1. Quadflieg, T.; Leimbrink, S.; Gries, T.; Stolyarov, O. Effect of coating type on the mechanical performance of warp-knitted fabrics and cement-based composites. *J. Compos. Mater.* **2018**, *52*, 1–14. [CrossRef]
2. Dvorkin, D.; Poursaee, A.; Peled, A.; Weiss, W.J. Influence of bundle coating on the tensile behavior, bonding, cracking and fluid transport of fabric cement-based composites. *Cement Concr. Compos.* **2013**, *42*, 9–19. [CrossRef]
3. D'Antino, T.; Papanicolaou, C. Mechanical characterization of textile reinforced inorganic-matrix composites. *Compos. B Eng.* **2017**, *127*, 78–91. [CrossRef]
4. Kulas, C.; Gmbh, S. *Actual Applications and Potential of Textile-Reinforced Concrete*; GRC: Dubai, The United Arab Emirates, 2005.
5. Rossi, E.; Randl, N.; Harsányi, P.; Mészly, T. Experimental study of fibre-reinforced TRC shear strengthening applications on non-stirrup reinforced concrete T-beams. *Eng. Struct.* **2022**, *256*, 113923. [CrossRef]
6. Mesticou, Z.; Bui, L.; Larbi, A.S. Experimental investigation of tensile fatigue behavior of Textile-Reinforced Concrete (TRC): Effect of fatigue load and strain rate. *Compos. Struct.* **2017**, *160*, 1136–1146. [CrossRef]
7. Zhou, F.; Liu, H.; Du, Y.; Liu, L.; Zhu, D.; Pan, W. Uniaxial Tensile Behavior of Carbon Textile Reinforced Mortar. *Materials* **2019**, *12*, 374. [CrossRef]
8. Younis, A.; Ebead, U.A.; Shrestha, K.C. Tensile characterization of multiply fabric-reinforced cementitious matrix strengthening systems. *Struct. Concr.* **2020**, *21*, 713–723. [CrossRef]
9. Goliath, K.B.; Cardoso, D.C.; Silva, F.A. Flexural behavior of carbon-textile-reinforced concrete I-section beams. *Compos. Struct.* **2021**, *260*, 113540. [CrossRef]
10. Chandrathilaka, E.; Baduge, S.K.; Mendis, P.; Thilakarathna, P. Flexural Performance of Prefabricated Ultra-High-Strength Textile Reinforced Concrete (UHSTRC): An Experimental and Analytical Investigation. *Buildings* **2020**, *10*, 68. [CrossRef]
11. Harri, G.; Gokulnath, N.; Karthick, R. Flexural Strengthening of Reinforced Concrete Beams using Ferrocement by Basalt Reinforcing Mesh. *J. Civ. Eng. Environ. Technol.* **2015**, *2*, 668–671.
12. Jiang, Y.; Wang, X.; Li, B.; Higashi, Y.; Taniguchi, K.; Koga, D.; Ishida, K. Tunnel reinforcement effects by using combined PCM shotcrete and FRP grid technique. In Proceedings of the ISRM International Symposium-8th Asian Rock Mechanics Symposium, Sapporo, Japan, 14–16 October 2014.
13. Li, C.; Xian, G. Experimental investigation of the microstructures and tensile properties of polyacrylonitrile-based carbon fibers exposed to elevated temperatures in air. *J. Eng. Fiber. Fabr.* **2019**, *14*, 155892501985001. [CrossRef]
14. Feih, S.; Mouritz, A.P. Tensile properties of carbon fibers and carbon fiber–polymer composites in fire. *Compos. Part A—Appl. Sci. Manuf.* **2012**, *43*, 765–772. [CrossRef]
15. Ombres, L.; Mazzuca, P.; Verre, S. Effects of Thermal Conditioning at High Temperatures on the Response of Concrete Elements Confined with a PBO-FRCM Composite System. *J. Mater. Civ. Eng.* **2022**, *34*, 04021413. [CrossRef]
16. Nanni, A. FRCM strengthening—A new tool in the concrete and masonry repair toolbox. *Concr. Int. Des. Constr.* **2012**, *34*, 43–49.
17. Estevan, L.; Varona, F.B.; Baeza, F.J.; Torres, B.; Bru, D. Textile Reinforced Mortars (TRM) tensile behavior after high temperature exposure. *Constr. Build. Mater.* **2022**, *328*, 127116. [CrossRef]

18. Xu, S.; Shen, L.; Wang, J. The high-temperature resistance performance of TRC thin-plates with different cementitious materials: Experimental study. *Constr. Build. Mater.* **2016**, *115*, 506–519. [CrossRef]
19. Ferretti, F.; Tilocca, A.R.; Incerti, A.; Mazzotti, C.; Savoia, M. Effects of Thermal Variations on the Tensile Behavior of FRCM Strengthening Systems. *J. Compos. Constr.* **2022**, *26*, 4022067. [CrossRef]
20. Rambo, D.S.; Silva, F.A.; Filho, R.T.; Gomes, O.M. Effect of elevated temperatures on the mechanical behavior of basalt textile reinforced refractory concrete. *Mater. Des.* **2015**, *65*, 24–33. [CrossRef]
21. Rambo, D.S.; Yao, Y.; Silva, F.A.; Filho, R.T.; Mobasher, B. Experimental investigation and modelling of the temperature effects on the tensile behavior of textile reinforced refractory concretes. *Cement Concr. Compos.* **2017**, *75*, 51–61. [CrossRef]
22. Dinh, N.H.; Park, S.; Choi, K. Effect of dispersed micro-fibers on tensile behavior of uncoated carbon textile-reinforced cementitious mortar after high-temperature exposure. *Cement Concr. Compos.* **2021**, *118*, 103949. [CrossRef]
23. Nguyen, T.H.; Vu, X.H.; Larbi, A.S.; Ferrier, E. Experimental study of the effect of simultaneous mechanical and high-temperature loadings on the behavior of textile-reinforced concrete (TRC). *Constr. Build. Mater.* **2016**, *125*, 253–270. [CrossRef]
24. Rambo, D.S.; Silva, F.A.; Filho, R.T.; Ukrainczyk, N.; Koenders, E. Tensile strength of a calcium-aluminate cementitious composite reinforced with basalt textile in a high-temperature environment. *Cement Concr. Compos.* **2016**, *70*, 183–193. [CrossRef]
25. Homoro, O.; Vu, X.H.; Ferrier, E. Experimental and analytical study of the thermo-mechanical behavior of textile-reinforced concrete (TRC) at elevated temperatures: Role of discontinuous short glass fibers. *Constr. Build. Mater.* **2018**, *190*, 645–663. [CrossRef]
26. Tlaiji, T.V.; Vu, X.; Ferrier, E.; Larbi, A.S. Thermomechanical behavior and residual properties of textile reinforced concrete (TRC) subjected to elevated and high temperature loading Experimental and comparative study. *Compos. B Eng.* **2018**, *144*, 99–110. [CrossRef]
27. Hulin, T.; Lauridsen, D.H.; Hodicky, K.; Schmidt, J.W.; Stang, H. Influence of Basalt FRP Mesh Reinforcement on High-Performance Concrete Thin Plates at High Temperatures. *J. Compos. Constr.* **2015**, *20*, 04015034. [CrossRef]
28. *EN 1991-1-2*; Eurocode 1: Actions on Structures—Part 1–2: General Actions-Actions on Structures Exposed to Fire. European Committee for Standardization: Brussels, Belgium, 2002.
29. Lopresto, V.; Leone, C.; Iorio, D.I. Mechanical characterization of basalt fiber reinforced plastic. *Compos. B Eng.* **2011**, *42*, 717–723. [CrossRef]
30. Sim, J.; Park, C.; Moon, D.Y. Characteristic of basalt fiber as strengthening material for concrete structures. *Compos. B Eng.* **2005**, *36*, 504–512. [CrossRef]
31. Elmesalami, N.; Abed, F.; Refai, A.E. Concrete Columns Reinforced with GFRP and BFRP Bars under Concentric and Eccentric Loads: Experimental Testing and Analytical Investigation. *J. Compos. Constr.* **2021**, *25*, 04021003. [CrossRef]
32. *ISO 10618*; Carbon Fiber—Determination of Tensile Properties of Resin-Impregnated Yarn. ISO: Geneva, Switzerland, 2004.
33. *GB 50016*; Code for Design of Building Fire Protection. Ministry of Construction of the PRC: Beijing, China, 2014.
34. Zhang, X.; Wang, X.; Peng, Z.; Zhu, Z.; Wu, Z. Parametric study on mechanical properties of basalt leno textile applied as concrete reinforcement. *Adv. Struct. Eng.* **2022**, *25*, 48–62. [CrossRef]
35. Tian, L.; Zhang, J.; Dong, S.; Yuan, G.; Zhang, Q. Study on mechanical properties of cementitious composites reinforced with PVA fibers after exposure to high temperatures. *Concrete* **2011**, *28*, 31–33.
36. Lion, M.; Skoczylas, F.; Lafhaj, Z.; Sersar, M. Experimental study on a mortar. Temperature effects on porosity and permeability. Residual properties or direct measurements under temperature. *Cement Concr. Res.* **2005**, *35*, 1937–1942. [CrossRef]
37. Hager, I. Behavior of cement concrete at high temperature. *Bull. Pol. Acad.* **2013**, *61*, 145–154.
38. Silva, F.A.; Butler, M.; Hempel, S.; Filho, R.T.; Mechtcherine, V. Effects of elevated temperatures on the interface properties of carbon textile-reinforced concrete. *Cement Concr. Compos.* **2014**, *48*, 26–34. [CrossRef]